https://doi.org/10.5194/egusphere-2022-294
Preprint. Discussion started: 25 May 2022

Wind work at the air-sea interface: A Modeling Study in Anticipation of Future Space Missions

Hector S. Torres[1], Patrice Klein[1,2,3], Jinbo Wang[1], Alexander Wineteer[1], Bo Qiu[4], Andrew F. Thompson[2], Ernesto Rodriguez[1], Dimitris Menemenlis[1], Andrea Molod[5], Christopher N. Hill[6], Ehud Strobach[7], Hong Zhang[1], Mar Flexas[2], and Dragana Perkovic-Martin[1]

[1]Jet Propulsion Laboratory, California Institute of Technology, Pasadena, CA, USA
[2]Environmental Science and Engineering, California Institute of Technology, Pasadena, CA, USA
[3]LMD/IPSL, CNRS, Ecole Normale Supérieure, PSL Research University, 75005 Paris, France
[4]University of Hawaii, Honolulu, HI, USA
[5]NASA Goddard Space Flight Center, MD, USA
[6]Earth, Atmospheric and Planetary Sciences, Massachusetts Institute of Technology, MA, USA
[7]Agricultural Research Organization, Israel

Correspondence: Hector S. Torres (Hector.Torres.Gutierrez@jpl.nasa.gov)

Abstract.

Wind work at the air-sea interface is the transfer of kinetic energy between the ocean and the atmosphere and, as such, is an important part of the atmosphere-ocean coupled system. Since wind work involves winds and ocean currents that span a broad range of spatial and temporal scales, a comprehensive study would require access to observations of a wide range of space and time scales. In the absence of appropriate global observations, our study makes use of a new, global, coupled ocean-atmosphere simulation with horizontal grid spacing of 2–5 km for the ocean and 7 km for the atmosphere. Here we develop a methodology, both in physical and spectral space, to diagnose different components of wind work in terms of forcing distinct classes of oceanic motions, including mean currents, time-dependent large-scale currents and mesoscale eddies, and internal gravity waves such as near-inertial waves. The total simulated wind work has a magnitude of 5.21 TW, a value much larger than reported by previous modeling studies. The total wind work is first decomposed into time-mean and time-dependent components, with the former accounting for 2.23 TW (43%) and the latter 2.98 TW (57%). The time-dependent wind work is then decomposed into two components, a high-frequency component that forces internal gravity waves and a low-frequency component that forces mesoscale eddies and large-scale currents. The high-frequency component is positive at scales between 10 km and 1000 km and represents 75% of the total time-dependent component. The low-frequency component is found to be positive for spatial scales larger than 275 km and ten times larger than the negative part associated with smaller spatial scales. The negative wind work acts as a surface drag that slows down surface currents and damps mesoscale eddies whereas the positive low-frequency part accelerates large-scale currents. The complex and consequential interplay of surface winds and currents in the numerical simulation motivates the need for a winds-and-currents satellite mission to directly observe these wind work components.

1 Introduction

The diagnosis of wind work by the atmosphere on the ocean requires access to ocean-surface wind stress and currents. The wind stress vector, $\boldsymbol{\tau}$, can be written as

$$\boldsymbol{\tau} = \rho_{air} C_d |\mathbf{U_a} - \mathbf{u_o}|(\mathbf{U_a} - \mathbf{u_o}), \tag{1}$$

where ρ_{air} is the air density, C_d a drag coefficient, $\mathbf{U_a}$ the vector wind, and $\mathbf{u_o}$ the ocean-surface current vector (Large and Yeager, 2004). The wind work is the scalar product

$$F_s = \boldsymbol{\tau} \cdot \mathbf{u_o} = \rho_{air} C_d |\mathbf{U_a} - \mathbf{u_o}|(\mathbf{U_a} - \mathbf{u_o}) \cdot \mathbf{u_o} \tag{2}$$

Equation 2 highlights the strong nonlinear relationship of wind work with winds and currents. The present study focuses on the impact of wind work on the forcing of near-inertial motions, mesoscale eddies, and large-scale currents and gyres, as opposed to, for example, the generation of surface gravity waves, Langmuir circulation, and mixed layer turbulence.

Wind work at the air-sea interface is known to drive a large part of ocean dynamics. For example, wind work forces equatorial and tropical zonal jets (spatial scales of 1000 km and time scales of days to months), which are key players in the El Niño Southern Oscillation (ENSO) (Ferrari and Wunsch, 2009). Wind work also forces, at mid-latitudes, mean currents and large eddies (spatial scales $>$ 500 km and time scales of days to months). It impacts mesoscale ocean eddies at mid-latitudes (spatial scales $<$ 500 km and time scales of days to months) and therefore the horizontal and vertical transport of heat at these latitudes (Eden and Dietze, 2009; Zhai et al., 2012; Zhai, 2013; Klein et al., 2019; Rai et al., 2021). Additionally, wind work generates near-inertial waves and internal gravity waves (spatial scales of 10 to 1000 km and time scales of hours), which contribute to ocean mixing in the ocean interior and therefore to the Meridional Overturning Circulation (MOC) (Komori et al., 2008; Polzin and Lvov, 2011; Nikurashin et al., 2013; Alford et al., 2016).

An example of the multiscale issues we have to address is the following. Wind fluctuations with time scales of one hour impact the wind stress at these short time scales. The resulting wind work, in regions of atmospheric storm tracks, generates near-inertial motions and internal gravity waves (with time scales less than a day) whose kinetic energy can be up to twice larger than when only wind fluctuations with time scales longer than six hours are considered (Klein et al., 2004; Rimac et al., 2013). However, wind fluctuations at short time scales also impact the weekly-averaged and monthly-averaged wind stress and therefore the wind work at these longer time scales. This is due to the quadratic relationship between winds and wind stress (Eq. 1). For example, in regions of atmospheric storm tracks, the resulting monthly-averaged wind work is larger by a factor four when wind fluctuations at short time scales are taken into account than when only weekly or monthly winds are used (Zhai et al., 2012; Zhai, 2017). Thus high-frequency winds can lead to a larger forcing of the time-mean ocean currents and therefore to the generation of mesoscale eddies with low frequency when these currents are unstable. This example and the more detailed arguments developed in Section 3 emphasize the need to have observations of winds and currents over a broad range of time and spatial scales in order to diagnose the different wind-work components that force or damp oceanic motions.

To take into account these scale interactions and their impact on wind work, we make use of model output from a new, global, Coupled Ocean-Atmosphere Simulation (COAS) that includes tidal forcing in the ocean and has horizontal grid spacing of 2–5 km in the ocean and 7 km in the atmosphere. This simulation produces wind and current fluctuations at very short time scales (45-s ocean-atmosphere coupling time step) and enables spatial collocation and contemporaneity of atmospheric winds and ocean currents. To further understand the impact of high-frequency wind fluctuations, COAS results are compared to those obtained from an ocean-only simulation that has a similar configuration as the ocean component of the COAS simulation but forced by prescribed 6-hourly atmospheric fields. The present study makes use of a simple methodology in physical and spectral spaces to better identify the impact of these scale interactions on wind work. The next section describes the global numerical model used. Section 3 describes the methodology employed and discusses the multiscale issue we have to address. An analysis of the wind work components that force different classes of motion is presented in Section 4. Conclusions follow in Section 5.

2 Numerical simulations: Coupled ocean-atmosphere vs. forced ocean

The new, global, Coupled Ocean-Atmosphere Simulation (COAS) used in this study comprises the Goddard Earth Observing System (GEOS) atmospheric and land model coupled to an ocean configuration of the Massachusetts Institute of Technology general circulation model (MITgcm). The configuration of COAS used in this study is identical to that used in the studies of Strobach et al. (2020, 2022) except that the ocean model includes tidal forcing, which triggers the generation of internal tides and promotes a more realistic internal gravity wave continuum.

The GEOS model was configured to use the C1440 cubed-sphere grid, which has nominal horizontal grid spacing of 6.9 km. The vertical grid type is hybrid sigma-pressure with 72 levels. A detailed description of the GEOS atmospheric model configuration used in COAS is found in Molod et al. (2015) and Strobach et al. (2020). The surface layer parameterisation of turbulent fluxes is a modified version of the parameterisation documented in Helfand and Schubert (1995), with a wind stress and surface roughness model modified by the updates of Garfinkel et al. (2011) for a mid-range of wind speeds, and further modified by the updates of Molod et al. (2013) for high winds.

The MITgcm component of COAS uses the Latitude-Longitude-polar-Cap 2160 (LLC2160) configuration described in Arbic et al. (2018) and previously used in the studies of Flexas et al. (2019), Su et al. (2018), and many others. The LLC2160 solves the hydrostatic primitive equations for velocity, potential temperature, and salinity with a seawater equation of state. The finite

https://doi.org/10.5194/egusphere-2022-294
Preprint. Discussion started: 25 May 2022

volume method is used to discretize the equations in space. The LLC2160 configuration uses an implicit free surface, real freshwater surface forcing, and the K-Profile Parameterization (KPP) vertical mixing scheme of Large et al. (1994) but with the non-local term disabled. The LLC2160 has nominal horizontal grid spacing of 1/24°, ranging from 2.3 km in the Arctic Ocean, 4.6 km at the Equator, and 1.7 km at the southernmost location around Antarctica. There are 90 vertical levels with 1-m vertical grid spacing at the surface, gradually increasing to ∼300 m near the 5000-m depth. The integration time step for the GEOS C1440 and the MITgcm LLC2160 components and the coupling time step for the coupled C1440-LLC2160 COAS model is 45 seconds.

The COAS simulation was initialized on January 20 using 2012 ocean initial conditions from the forced LLC2160 MITgcm simulation and 2020 atmospheric initial conditions from the Modern-Era Retrospective analysis for Research and Applications, Version 2 (MERRA-2) interpolated to the C1440 GEOS grid. The results shown in this study are based on the first 111 days of simulation, from January 20 to May 9, which was all the output available at the time this study was initiated. The COAS simulation now extends for a period of 14 months (January 20, 2020 to March 25, 2021). Model output includes hourly three-dimensional fields for all oceanic and atmospheric variables, some higher-frequency (15-minute) two-dimensional atmospheric fields, and many diagnostic variables, for a total storage requirement of ∼3 Petabytes.

In addition to the C1440-LLC2160 COAS simulation, our study also used 111 days (January 20 to May 9, 2012) of model output from the forced LLC2160 simulation. The ocean-only LLC2160 simulation was forced by six-hourly atmospheric conditions from the 0.14-degree European Center for Medium-Range Weather Forecasts (ECMWF) atmospheric operational model analysis, starting in 2011. Although both the COAS and forced LLC2160 simulations include full lunisolar tidal forcing, tidal forcing in the forced LLC2160 simulation was inadvertently overestimated by a factor of 1.1121. Since the forced LLC2160 simulation was used to initialize COAS, both simulations have identical January-20 initial conditions. As described in Rocha et al. (2016), the LLC2160 ocean simulation was initialized from a coarser-resolution (1/12°) simulation, which itself was initialized from a data-constrained simulation with 1/6° nominal grid spacing provided by the Estimating the Circulation and Climate of the Ocean, Phase II (ECCO2) project (Menemenlis et al., 2008).

3 Methodology in physical and spectral spaces

3.1 Winds and ocean currents in physical space

The wind work is diagnosed from the outputs of wind stresses and ocean currents produced by the coupled simulation. These outputs are decomposed into different components in terms of time and spatial scales, with this decomposition based on the time and spatial variability of winds and currents.

Figures 1a and b show a snapshot of the wind stress and oceanic currents in the global ocean. Movies of these two key variables are available in https://doi.org/10.5281/zenodo.6478679. The wind stress (Figure 1a) is usually large-scale, $\mathcal{O}(1000\text{ km})$, re-

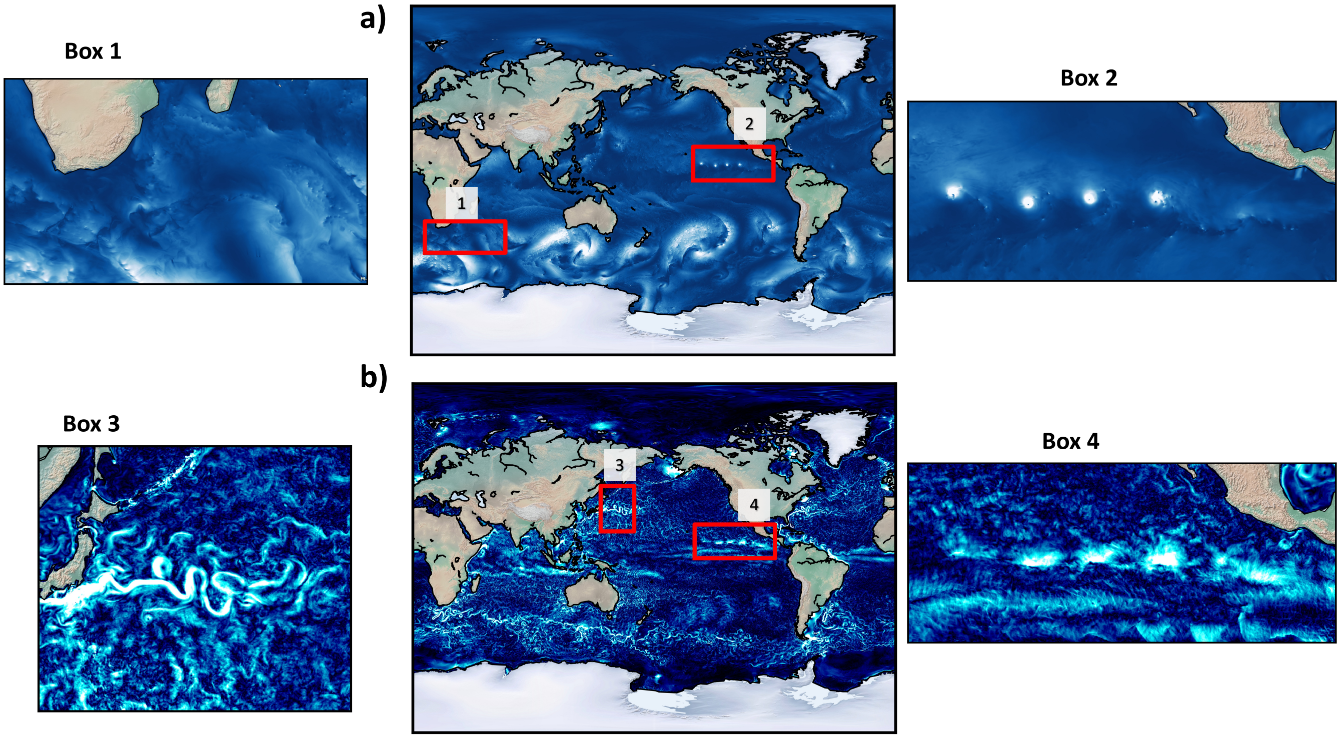

Figure 1. (a) Surface wind stress and (b) ocean-surface currents in the Coupled Ocean-Atmosphere Simulation (COAS) during austral winter.

sulting from atmospheric weather patterns that propagate fast, for example, going from South Africa to South America within 6–10 days (Figure 1a). These large-scale patterns are embedded with small-scale patterns (as small as 100 km), some of them propagating with the large-scale ones, others being quasi-stationary (see Box 1 on Figure 1a and the movie). The latter are mostly the signature of mesoscale ocean eddies on the wind stress and can be identified from watching the movie. Impact of land topography on the wind stress is also noticeable in the movies, in particular close to the East coast of Asia at mid-latitudes and the West coast of Mexico at the equator. The latter may lead to the formation of hurricanes, such as those noticeable in Box 2 of Figure 1a. Energetic ocean currents (Figure 1b) are characterized by very small scales contrary to the wind stress and are moving very slowly as revealed by the movie (see also Box 3 on Figure 1b). These motions are mostly associated with wavy/unstable baroclinic mean currents and eddies. Zonal jets are noticeable at the equator and in tropical regions (Figure 1b). Not surprisingly, hurricanes have a strong signature on surface currents (Box 4 on Figure 1b). Ocean current patterns with larger scales, but less energetic than small-scale currents, are also noticeable in the movie. These patterns propagate with large-scale atmospheric storms. They are the signature of near-inertial motions and internal waves driven by the large-scale winds stress.

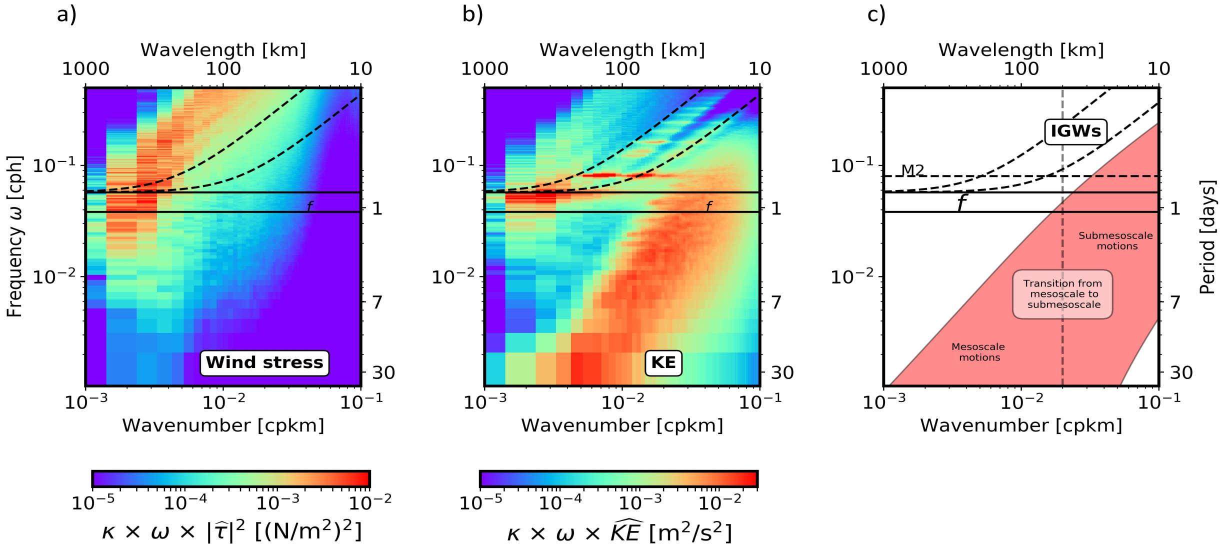

Figure 2. COAS frequency-wavenumber spectra of (a) surface wind stress and (b) surface currents in the Kuroshio Extension region. Panel (c) is a Stommel Diagram of oceanic motions (see text). The dashed lines in the three panels show the linear dispersion relation curves for internal gravity waves associated with the first four baroclinic modes, which helps to identify energetic internal gravity waves. See Torres et al. (2018) and Qiu et al. (2018) for a detailed explanation of the above partition.

3.2 Winds and ocean currents in spectral space

These different time and spatial scales of wind stresses and ocean currents are further characterized in spectral space in regional domains. Figure 2 shows spectra of wind stresses and currents in the Kuroshio Extension region in the North Pacific (see Appendix A for spectra calculation details). The displayed frequency and wavenumber ranges span, respectively, periods between 2 hours and 40 days and length scales from 10 km to 1000 km. Wind stresses and currents occupy different regions in the spectral space. On the one hand, wind stresses (Figure 2a) are mostly characterized by high frequencies ($<$ 2 days) comprised of large spatial scales ($>$500 km) for time scales larger than 12 hours and small spatial scales (20–500 km) for time scales smaller than 12 hours. Such wind stresses are the signature of large-scale atmospheric storms and the associated small-scale patterns that propagate with them. Small-scale wind stress patterns associated with slowly-moving ocean eddies are much weaker and occupy periods larger than 2 days. On the other hand, energetic ocean currents (Figure 2b) are mostly characterized by smaller spatial scales ($<$500 km) and lower frequencies (periods $>$2 days). As sketched in Figure 2c, these currents are associated with large and mesoscale eddies known to be driven by the baroclinic instability of mean currents. However, ocean currents also have a large magnitude in the near-inertial band ($\omega \approx f$) with scales larger than 500 km. These currents are associated with near-inertial waves (see Figure 2c) forced by high-frequency winds.

Based on the properties discussed above, we consider the following decomposition for surface wind stress $\boldsymbol{\tau}$ and ocean-surface currents $\mathbf{u_o}$:

$$\mathbf{X} = \overline{\mathbf{X}} + \mathbf{X}'_{hf} + \mathbf{X}'_{lf>} + \mathbf{X}'_{lf<}\,, \tag{3}$$

where $\mathbf{X}$ represents either $\boldsymbol{\tau}$ or $\mathbf{u_o}$, the overline operator represents a time-average over 3.5 months, and the prime operator represents time fluctuations with periods smaller than 3.5 months. The time fluctuations are further decomposed into a high-frequency component (hf) for periods smaller than 5 days and a low-frequency component (lf) for periods between 5 days and 3.5 months. Varying the 5-day threshold between low-frequency and high-frequency motions does not have a significant impact on the results of the present study. The hf component captures high-frequency contributions such as those at the inertial frequency. The low-frequency component is further decomposed into two contributions in terms of spatial scales: the large-scale contribution ($lf >$) for spatial scales larger than a critical length scale L_c and the small-scale contribution ($lf <$) for scales smaller than L_c. Following Rai et al. (2021), we define L_c as the length scale for which the low-frequency component of wind work is negative for scales smaller than L_c and positive for larger scales. Negative wind work at these scales is what is called "eddy killer" or "eddy damping", a mechanism that has been thoroughly investigated during the past 15 years (Eden and Dietze, 2009; Renault et al., 2016, 2018; Rai et al., 2021). Using the same procedure as Rai et al. (2021), we found that $L_c \approx 300$ km (see Section 4.3 for more details).

3.3 Analysis of the wind work

The wind work depends not only on the amplitudes of time-mean and fluctuating surface wind stress and currents but also on their cross-correlation. We apply the Reynolds decomposition to Eq. 2 using Eq. 3. The resulting wind work at each grid point averaged over 3.5 months includes a time-mean component ($\overline{\boldsymbol{\tau}}.\overline{\mathbf{u_o}}$) and a total time-dependent component ($\overline{\boldsymbol{\tau}'.\mathbf{u_o}'} = \overline{\boldsymbol{\tau}'_{hf}.\mathbf{u_o}'_{hf}} + \overline{\boldsymbol{\tau}'_{lf>}.\mathbf{u_o}'_{lf>}} + \overline{\boldsymbol{\tau}'_{lf<}.\mathbf{u_o}'_{lf<}}$), such that

$$\overline{F_s} = \overline{\boldsymbol{\tau}}.\overline{\mathbf{u_o}} + \overline{\boldsymbol{\tau}'_{hf}.\mathbf{u_o}'_{hf}} + \overline{\boldsymbol{\tau}'_{lf>}.\mathbf{u_o}'_{lf>}} + \overline{\boldsymbol{\tau}'_{lf<}.\mathbf{u_o}'_{lf<}}\,. \tag{4}$$

First, we have checked the validity of the Reynolds decomposition by estimating the order of magnitude of each cross term not present in Eq. 4. Their order of magnitude is 10^{-16} smaller than the terms present in Eq. 4 (see Figure 3), which confirms the pertinence of our decomposition. The four terms on the right hand side (RHS) of Eq. 4 identify the contribution of the different time and spatial scales of the wind stress and current to the wind work averaged over three months. Each term in Eq. 4 associated with a given class of time and spatial fluctuations directly forces surface currents corresponding to the same class as explained in Appendix B. Thus, the first right hand side (RHS) term in Eq. 4 should force mean currents ($\overline{\mathbf{u_o}}$), the second one, mostly near-inertial waves and internal gravity waves ($\mathbf{u_o}'_{hf}$), the third one, large-scale currents and gyres ($\mathbf{u_o}'_{lf>}$), and the last one, mesoscale eddies ($\mathbf{u_o}'_{lf<}$).

However, each class of motions can be indirectly forced by the wind work associated with other time and spatial scales. This is due to the presence of the nonlinear advection terms in the momentum equations (see also Appendix B). Let us consider for

https://doi.org/10.5194/egusphere-2022-294
Preprint. Discussion started: 25 May 2022

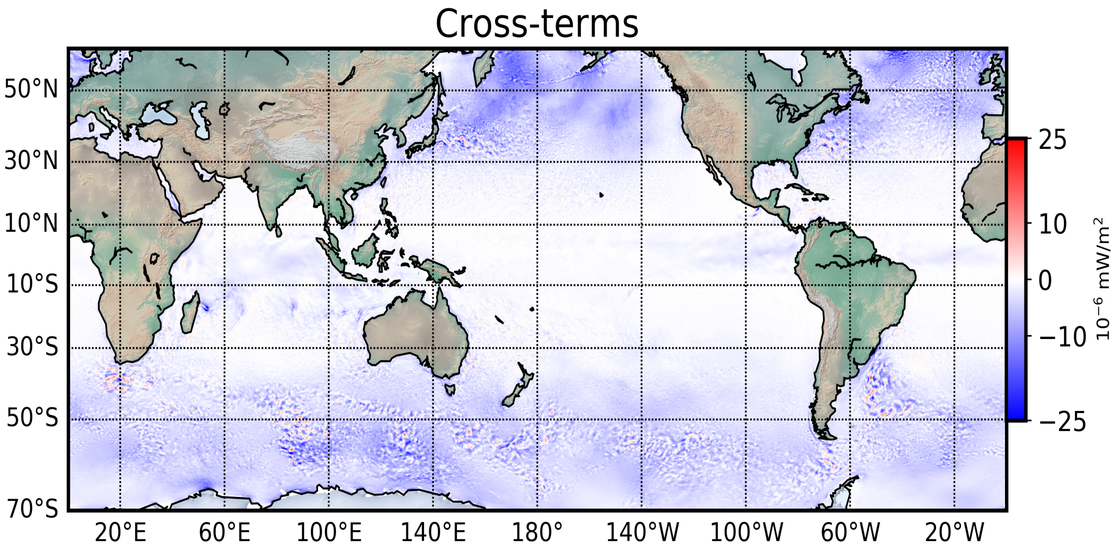

Figure 3. RMS values of all the cross terms not present in Eq. 4

example the equations for the time evolution of $\mathbf{u_o}'_{lf<}$ and $\mathbf{u_o}'_{lf>}$ where only nonlinear advection terms related to $\mathbf{u_o}'_{lf<}$ and $\mathbf{u_o}'_{lf>}$ are retained for the sake of simplicity (see Eq. B14 in Appendix B for a generalization,)

$$\frac{\partial \overline{\mathbf{u_o}'^2_{lf<}}/2}{\partial t} \sim -\overline{\mathbf{u_o}'_{lf<}.\mathbf{u_o}'_{lf<}.\nabla\mathbf{u_o}'_{lf>}} - \overline{\mathbf{u_o}'_{lf<}.\mathbf{u_o}'_{lf<}.\nabla\mathbf{u_o}'_{lf<}} - \overline{\mathbf{u_o}'_{lf>}.\mathbf{u_o}'_{lf<}.\nabla\mathbf{u_o}'_{lf<}} + \frac{\overline{\boldsymbol{\tau}'_{lf<}.\mathbf{u_o}'_{lf<}}}{H}, \tag{5}$$

$$\frac{\partial \overline{\mathbf{u_o}'^2_{lf>}}/2}{\partial t} \sim -\overline{\mathbf{u_o}'_{lf>}.\mathbf{u_o}'_{lf>}.\nabla\mathbf{u_o}'_{lf>}} - \overline{\mathbf{u_o}'_{lf>}.\mathbf{u_o}'_{lf<}.\nabla\mathbf{u_o}'_{lf<}} + \frac{\overline{\boldsymbol{\tau}'_{lf>}.\mathbf{u_o}'_{lf>}}}{H}. \tag{6}$$

H is a mixed-layer depth assumed to be constant. From Eq. 5, surface currents, $\mathbf{u_o}'_{lf<}$, are directly forced by $\boldsymbol{\tau}'_{lf<}.\mathbf{u_o}'_{lf<}$. However, these currents are also affected by the first RHS term in Eq. 5 that involves $\mathbf{u_o}'_{lf>}$. If currents, $\mathbf{u_o}'_{lf>}$, are unstable, production of surface currents at smaller spatial scales ($\mathbf{u_o}'_{lf<}$) can occur through this first RHS term. From Eq. 6, $\mathbf{u_o}'_{lf>}$ is directly forced by $\boldsymbol{\tau}'_{lf>}.\mathbf{u_o}'_{lf>}$. The consequence is that, through the first RHS term in Eq.5, $\mathbf{u_o}'_{lf<}$ is indirectly forced by $\boldsymbol{\tau}'_{lf>}.\mathbf{u_o}'_{lf>}$. Of course, scale interactions are more complex and involve more frequencies and spatial scales as discussed at the end of Appendix B (see Eq. B14). Such nonlinear interactions drive the kinetic energy transfer between scales (inverse and direct kinetic energy cascades) as well as current instabilities. However, the present example illustrates that, in order to understand the wind impact on the ocean dynamics, we need to consider the different components of the wind work displayed in Eq. 4 altogether, and not just focusing on one or two components. The present study analyses all wind work components. A more thorough future study should be dedicated to the kinetic energy budget in the upper oceanic layers that involves both wind work forcing and nonlinear advection of momentum.

https://doi.org/10.5194/egusphere-2022-294
Preprint. Discussion started: 25 May 2022

Table 1. Time-mean (TM) and time-dependent (TD) contributions to the wind work in TW from COAS and from LLC, over the World ocean and in terms of latitude band

Latitude band	COAS total	COAS TM	COAS TD	LLC total	LLC TM	LLC TD
Global	5.21	2.23	2.98	3.26	1.51	1.75
North of 30°N	1.06	0.2	0.86	0.52	0.11	0.41
$< \|30\|°$	1.96	1.2	0.76	1.32	0.81	0.51
South of 30°S	2.19	0.83	1.36	1.42	0.59	0.83

4 Multiscale decomposition of wind work

As indicated in Table 1, the total wind work ($\overline{F_s}$) over the 3.5 month period, January to April, is 5.21 TW in COAS simulation, a value much larger than reported in most of the previous papers ($\sim$2-3 TW, see Zhai (2017)). The wind work is only 3.26 TW in LLC2160 simulation, which reveals the strong impact of high-frequency wind fluctuations in COAS compared with LLC2160 simulation ($\sim$1 minute period instead of 6 hour period). We next examine how the total wind work is partitioned into the different components present in Eq. 4.

4.1 Time-mean component and total time-dependent component of the wind work

4.1.1 Time-mean component: $\overline{\boldsymbol{\tau}}.\overline{\mathbf{u}}_\mathbf{o}$

The time-mean component of the wind work (first term on the RHS of Eq. 4) represents 43% of the total wind work (Table 1). Figures 4a,c and e display the spatial distribution of this component from COAS and LLC2160 simulations. Values in COAS simulation are positive and larger by a factor 1.5 than in LLC2160 simulation in most regions (Figure 4c). This difference reaches a factor 2 in western boundary currents (WBCs), such as the Gulf Stream in the north Atlantic ocean and the Kuroshio Extension in the north Pacific ocean (see Table 1), and also in some regions of the equatorial/tropical band (see Figures 4a,c and e (differences between blue and orange curves)). This factor is only 1.4 in the southern hemisphere. Such differences again emphasize the impact of high-frequency wind fluctuations.

In both simulations (Figures 4a,c), wind work displays several zonal patterns elongated over $\sim$ 3000 km at tropical and equatorial latitudes, i.e. between 30°N and 30°S, mostly across the Indian, Pacific and Atlantic oceans with an intensification across the equator. Such wind work, known to be associated with trade winds, forces tropical and equatorial zonal jets (Maximenko et al., 2008; Chelton et al., 2011; Laurindo et al., 2017). Wind work is also intensified in the Antarctic Circumpolar Current (ACC) in the southern hemisphere, like around the longitude of 130°E, displaying elongated patterns at mesoscale (100–400 km). These elongated mesoscale patterns are usually explained as the signature of the wind stress forcing on stationary mesoscale eddies trapped by topography (Maximenko et al., 2008). As confirmed by Figure 4e, the time-mean component of

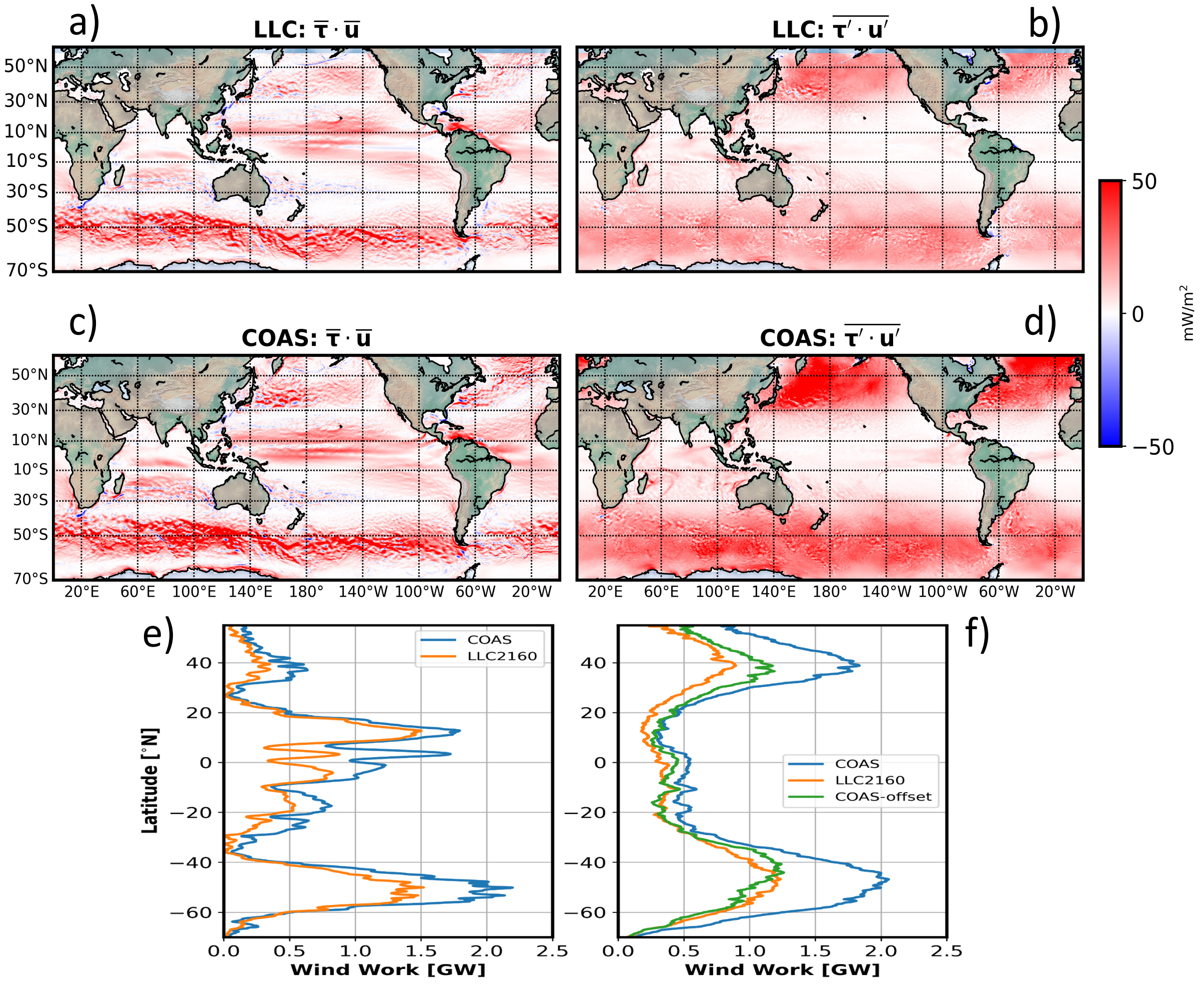

Figure 4. Wind work in mW/m^2 from LLC2160 simulation (a,b) and coupled simulation, COAS (c,d), computed using wind stress and surface currents averaged over 3 months (a,c) and using instantaneous wind stress and surface currents after removing their three month averaged values (b,d). (e,f) Zonally integrated wind work in GW from COAS (blue curves) and from LLC2160 (orange curves) when using wind stress and surface currents averaged over 3 months (e) and using instantaneous wind stress and surface currents after removing their three month averaged values (f). The green curve in (f) shows the wind work in COAS when an offset of 12 hours is applied between wind stresses and surface currents.

the wind work north of 30°N, is much smaller, displaying also zonally elongated patterns at mesoscale (100–400 km) (Figure 4c) often explained as the wind stress forcing on zonally propagating eddies in WBCs (Maximenko et al., 2008; Chelton et al., 2011). In summary, the time-mean component of the wind work dominates in the tropical and equatorial bands because of the trade winds and oceanic jets in these regions. It also dominates in the ACC because of the strong mean winds and stationary eddies. As such, this time-mean component is a mechanical forcing that strengthens tropical and equatorial zonal jets as well as stationary eddies in the ACC.

4.1.2 Total time-dependent component of the wind work: $\overline{\tau'.\mathrm{u_o}'}$

The total time-dependent component of the wind work is the addition of the second to fourth components in Eq. 4. It dominates the total wind work (57%) (Table 1) with a magnitude of 2.98 TW in COAS. From Figure 4d, this component, except in the ACC, totally differs from the time-mean component (Figure 4c). It is much weaker in tropical and equatorial regions (by a factor up to 3) and much larger at northern mid-latitudes by a factor larger than 3. In the global ocean, the total time-dependent component is 1.7 smaller in LLC2160 than in COAS. The difference between COAS and LLC2160 depends on latitude, as displayed by the zonally integrated wind work on Figure 4f (differences between blue and orange curves). This increase is larger by a factor 2 north of 30°N and 1.7 south of 30°N (see also Table 1). Increase at mid-latitudes is again the consequence of higher-frequency wind forcing in COAS than in LLC2160, in particular in the regions of atmospheric storm tracks. The next section examines the three components involved in the total time-dependent component of the wind work and their direct and indirect impacts on the ocean dynamics.

4.2 Low-frequency contribution to the wind work: $\overline{\tau'_{lf}.\mathrm{u_o}'_{lf}} = \overline{\tau'_{lf>}.\mathrm{u_o}'_{lf>}} + \overline{\tau'_{lf<}.\mathrm{u_o}'_{lf<}}$

Contribution of the low frequency component of the wind work, $\overline{\tau'_{lf}.\mathrm{u_o}'_{lf}}$, is shown on Figure 5c. This figure reveals patterns mostly located at mid-latitudes, with these patterns intensified in WBCs and in the ACC where eddies with scales smaller than 500 km are energetic (Figure 2b). However, wind work in the tropical and equatorial bands is not small (Figure 6b). Large RMS values of low-frequency currents in these regions (Figure 5a), may be interpreted in terms of tropical wave instabilities mostly driven by the interior ocean dynamics and not by the wind work, since RMS values of $\tau'_{lf_{rms}}$ are small at low latitudes (Figure 5b). Comparing Figures 4d and 5c indicates that magnitude of this low-frequency component is much smaller than the total time-dependent wind work. This result is understandable when examining Figures 2a and b : as mentioned before, wind stresses are weakly energetic in low-frequency regions whereas ocean currents are strongly energetic there. This differs from high-frequency regions, in particular in the near-inertial band at larger scales, where both winds and ocean currents are strongly energetic. Hence, we expected large wind work magnitude in high-frequency regions and much smaller one in low-frequency regions, which is what our results reveal: low-frequency wind work represents less than 25% of the time-dependent wind work and less than 14% of the total wind work.

https://doi.org/10.5194/egusphere-2022-294
Preprint. Discussion started: 25 May 2022

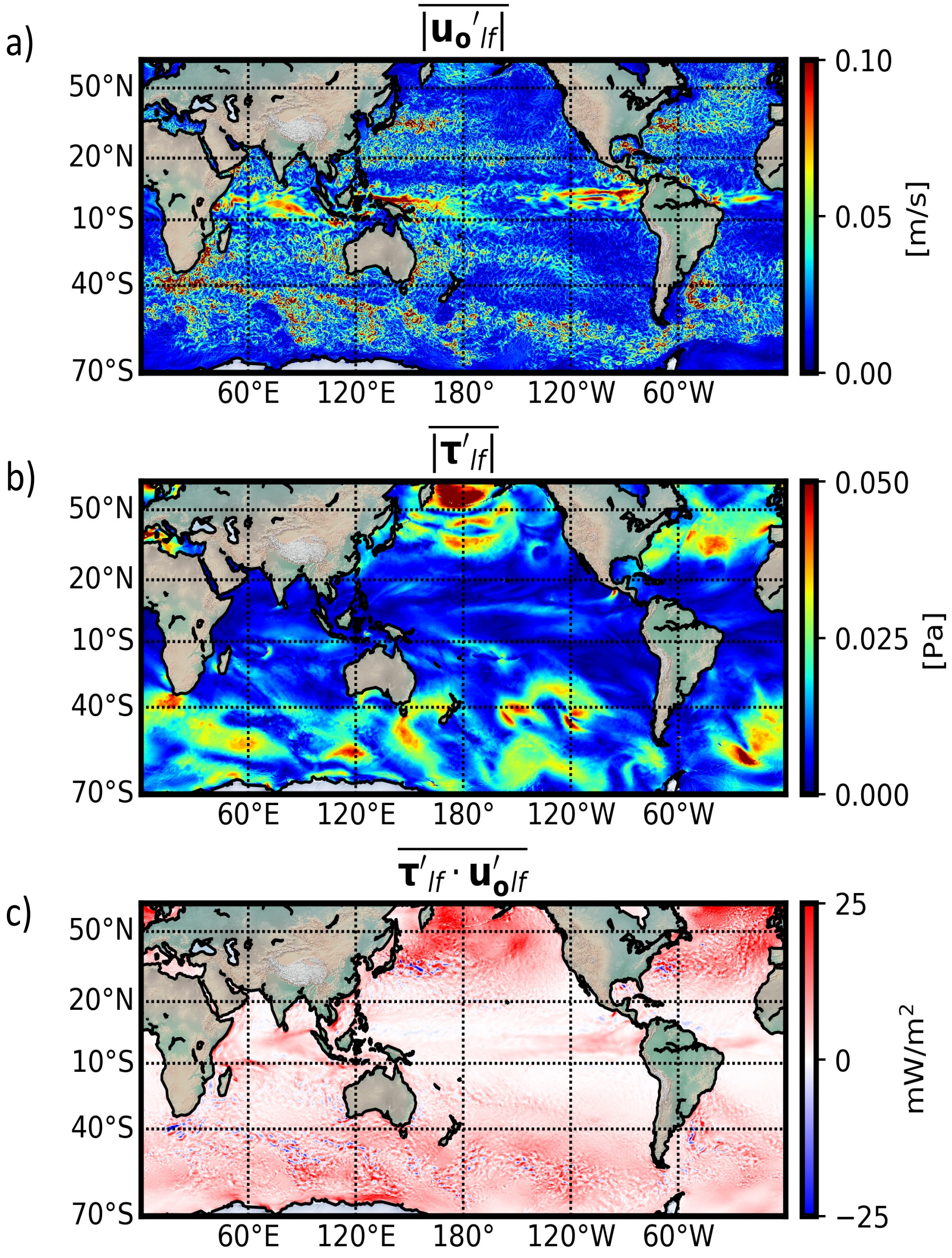

Figure 5. (a) RMS values, from COAS, of low-frequency ocean currents, $\overline{\mathbf{u_o}'_{lf}}$, and (b) RMS values of low-frequency wind stress, $\overline{\boldsymbol{\tau}'_{lf}}$. (c) low-frequency wind work, $\overline{\boldsymbol{\tau}'_{lf}.\mathbf{u_o}'_{lf}}$. The corresponding maps for LLC2160 (not shown) are similar except for the magnitude that is smaller.

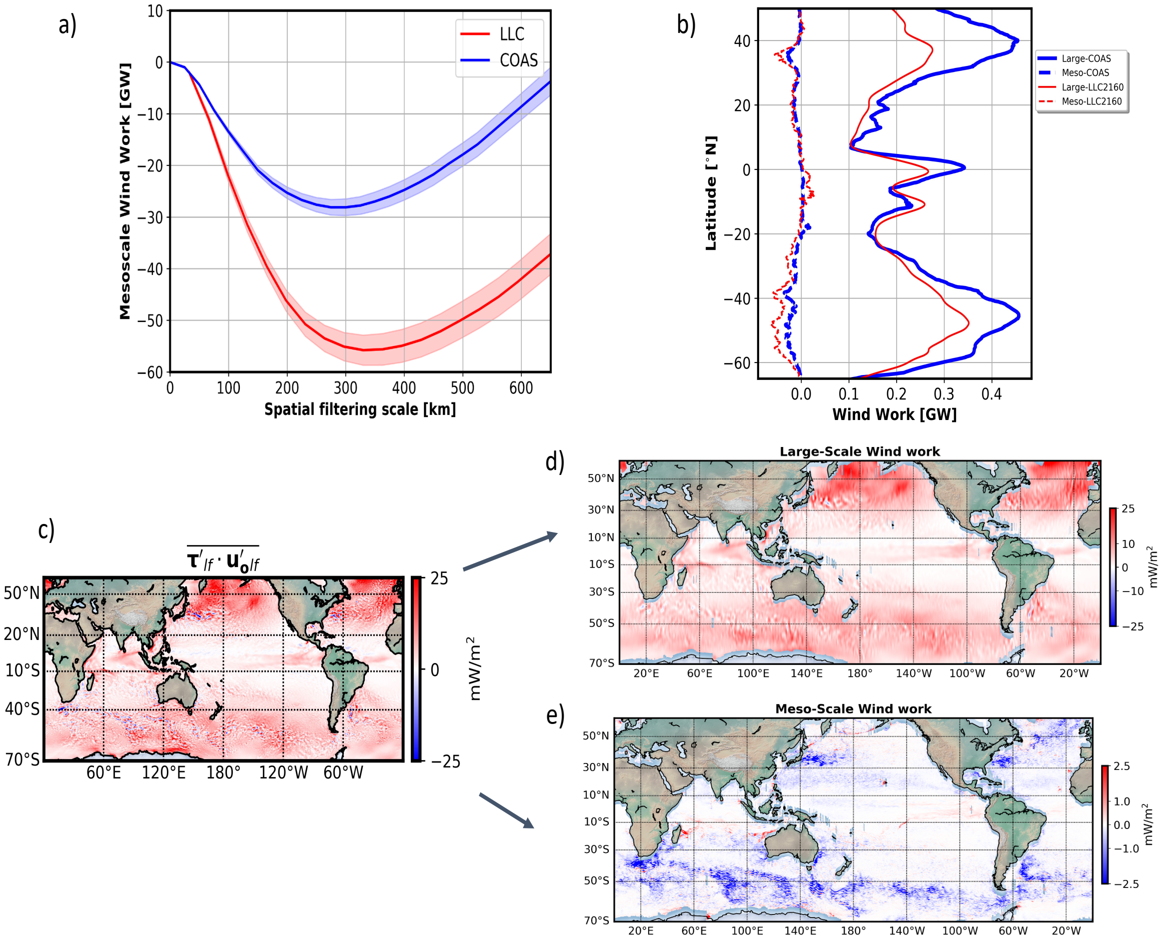

Figure 6. Low-frequency wind work. (a) Partition into positive and negative wind work. L_c is defined as the minimum of the blue (COAS) and red (LLC2160) curves (see Rai et al. (2021) for the calculation of these curves). Interpretation of L_c is that all wind work with scales smaller (larger) than L_c is negative (positive). (b) Zonally integrated low-frequency wind work with scales larger (solid curves) and smaller (dashed curves) than L_c from COAS (blue curves) and LLC2160 (red curves). (c,d,e) Distribution in physical space of the wind work from COAS for scales larger (d) and smaller (e) than L_c.

We now examine the low-frequency contribution decomposed in terms of spatial scales larger ($\overline{\boldsymbol{\tau}^{'}_{lf>}.\mathbf{u_o}^{'}_{lf>}}$) or smaller ($\overline{\boldsymbol{\tau}^{'}_{lf<}.\mathbf{u_o}^{'}_{lf<}}$) than L_c. To determine L_c, we follow the same methodology as Rai et al. (2021). The low-frequency oceanic currents and wind stress were subject to spatial decomposition by applying a "coarse-graining" approach (or low-pass filtered) (Aluie, 2019; Rai et al., 2021). The low-frequency field $\mathbf{X}'_{lf}$ is convoluted with a window function $\mathbf{G}_{>}$ (Top-Hat kernel, as proposed by Rai et al. (2021)) to define the low-frequency component with spatial scales larger than L_c: $\mathbf{X}'_{lf>} = \mathbf{G}_{>} * \mathbf{X}'_{lf}$, where $*$ is a convolution on a sphere a described in Aluie (2019). Once the low-frequency is decomposed in terms of spatial scales, then low-frequency contribution to the wind work of all spatial scales smaller than a given scale, L, has been estimated and it is shown on Figure 6a for the global ocean. As expected, the wind work is negative for small scales (Rai et al., 2021) and reaches a minimum at a critical length scale L_c equal to 275 km for COAS simulation and 340 km for LLC2160 simulation. This means that wind work for scales larger than L_c becomes positive. The negative wind work for scales smaller than L_c, i.e. $\overline{\boldsymbol{\tau}^{'}_{lf<}.\mathbf{u_o}^{'}_{lf<}}$, corresponds to the eddy damping effect explained and discussed by many studies (Eden and Dietze, 2009; Renault et al., 2016, 2018; Rai et al., 2021). An heuristic argument to explain the negative value of $\overline{\boldsymbol{\tau}^{'}_{lf<}.\mathbf{u_o}^{'}_{lf<}}$, is that wind is usually large scale and therefore an approximation of the wind stress and wind work at small scales is given by (using eqs. 1 and 2):

$$\begin{aligned} \boldsymbol{\tau}^{'}_{lf<} &\approx \rho_{air} C_d |U_a| (-\mathbf{u_o}^{'}_{lf<}), && (7) \\ \overline{\boldsymbol{\tau}^{'}_{lf<}.\mathbf{u_o}^{'}_{lf<}} &\approx -\rho_{air} C_d |U_a| \overline{|\mathbf{u_o}^{'}_{lf<}|^2} && (8) \end{aligned}$$

More detailed arguments are provided by Renault et al. (2018) and Rai et al. (2021).

Results from LLC2160 can be compared with those from Rai et al. (2021) since LLC2160, as Rai et al. (2021)'s observations, does not take into account the impact of high-frequency winds on low-frequency wind stress and neither the collocation and contemporaneity of winds and currents. In terms of eddy damping, wind work minimum in LLC2160 (Figure 6a) is similar to results from Rai et al. (2021) (∼57 GW). However, L_c from LLC2160 (∼340 km) is a little larger than found by Rai et al. (2021) (∼260 km). One possible interpretation is that on the one hand, Rai et al. (2021)'s study is based on AVISO products (https://resources.marine.copernicus.eu/?option=com_csw&task=results?option=com_csw&view=details&product_id=SEALEVEL_GLO_PHY_L4_REP_OBSERVATIONS_008_047) that concern ocean scales close to the first Rossby radius of deformation, i.e. scales not larger than 500 km in terms of eddy diameter (Chelton et al., 2011). On the other hand, ocean scales considered in our study concern a broader range, up to 1000-2000 km, which includes small and large eddies as well as wide ocean currents. This may explain the small scale-shift and therefore the larger L_c in LLC2160. Eddy damping is about twice smaller in COAS simulation (∼ 30 GW) than in LLC2160 simulation (∼ 57 GW). Such a difference can be explained by the impact of high-frequency winds on low-frequency wind stress as well as the collocation and contemporaneity of winds and currents (Zhai, 2013; Renault et al., 2016, 2018) taken into account in COAS.

Zonally integrated low-frequency contribution to the wind work is shown on Figure 6b. In COAS, the positive $\overline{\boldsymbol{\tau}^{'}_{lf>}.\mathbf{u_o}^{'}_{lf>}}$-part has a magnitude 10 times larger than the negative $\overline{\boldsymbol{\tau}^{'}_{lf<}.\mathbf{u_o}^{'}_{lf<}}$-part, a major difference that is also revealed by comparing Figures 6d and e. This difference is smaller in LLC2160 but still involves a factor 5 (Figure 6b). Both, positive and negative parts of the low-frequency contribution are mostly intensified at mid-latitudes as shown on Figures 6d and e. This positive part should force larger ocean eddies and wide currents. As emphasized by Chen et al. (2014) and Yang et al. (2021), shear and baroclinic instabilities of these large-scale currents and eddies may generate smaller-scale eddies. This suggests that production of smaller-scale eddies ($L < L_c$) by the positive part, $\overline{\boldsymbol{\tau}'_{lf>}.\mathbf{u_o}'_{lf>}}$, through instabilities, may be larger than the eddy damping as discussed in Section 3.2. Such comment points to the importance of taking into account the wind work components altogether, and not separately, to better infer the wind forcing of the ocean dynamics. It also emphasizes that a full kinetic energy budget should take into account all the wind work components as well as the nonlinear advection terms in the momentum equations, since the instabilities mentioned before are explained by these terms. Such kinetic energy budget should be the focus of a future study.

At last, comparison of LLC2160 results with those from Rai et al. (2021) reveals a major discrepancy in terms of the positive part of the low-frequency component of the wind work. In Rai et al. (2021), the positive part has a magnitude similar to that of the negative part (see their Figure 4H), whereas in LLC2160 the positive part is 5 times larger than the negative one (Figure 6b). Our interpretation, already mentioned before, is that Rai et al. (2021)'s observations of surface currents concern a small range of ocean scales whereas the much larger scale range of ocean currents considered in our study may significantly increase the positive part. We will further check this result in a future study, in particular in terms of regional variability, because of its importance on ocean eddy dynamics.

4.3 High-frequency component of the wind work: $\overline{\boldsymbol{\tau}'_{hf}.\mathbf{u_o}'_{hf}}$

From Eq. 3, the high-frequency component of the wind work is just the difference between the total time-dependent component (Figure 4d) and the low-frequency component (Figure 5c). Comparing Figures 4d and 5c indicates that the high-frequency component mostly dominates at mid-latitudes where the atmospheric storm tracks are located. Magnitude of this component increases from LLC2160 to COAS simulation by a factor 2.4 and 1.8, respectively in northern and southern hemispheres, which again highlights the impact of high-frequency winds. In COAS simulation, this component represents more than $\sim 75\%$ of the total time-dependent wind work and therefore more than $\sim 43\%$ of the total wind work.

High-frequency winds are expected to force currents principally at the inertial frequency since the ocean is an oscillator with the frequency f. A strong forcing means that near-inertial waves should be in phase with winds (Klein et al., 2004; Alford et al., 2016). To diagnose the phase relationship between high-frequency wind stresses and near-inertial waves and internal waves, we have re-estimated the total time-dependent component of the wind work by applying a phase lag between wind stresses and currents of 3, 6 and 12 hours. Results, displayed by the green meridional profile on Figure 4f for a time lag of 12 hours, are remarkable. There is a decrease of the total time-dependent component of the wind work by a a factor close to two at mid-latitudes in both hemispheres. Since the high-frequency component represents $\%75$ of the total time-dependent wind work, this means that 66% of the high-frequency component is explained by the forcing of near-inertial waves and internal gravity waves. Results with a time lag of 3 and 6 hours (not shown) are similar.

4.4 Wind work in oceanic regions

To further understand which classes of motions are forced or damped by the time-dependent components of the wind work, we focus again on the Kuroshio-Extension region (Figure 7). As before, results for other regions such as the Gulf Stream and the Antarctic Circumpolar Current, and in the tropical regions not much differ except for the magnitude (see Figure 8). This analysis is done in spectral space, using now a co-spectrum of the wind work (see methods). Figure 7a shows the wind work co-spectrum estimated from COAS simulation for spatial scales smaller than 800 km (see Appendix A for the calculation of the co-spectrum). As expected, the co-spectrum reveals a positive maximum around the inertial frequency, which corresponds to the forcing of near-inertial motions (Klein et al., 2004; Alford et al., 2016). Magnitude of the wind work for these high frequencies (in terms of period, T $<$2 days) is 52 mW/m2.

For time scales larger than 5 days, the wind work is negative (Figure 7a). This is related to the mesoscale eddy damping mentioned before, which concerns spatial scales up to 800 km in the Kuroshio (Figure 7a). Such large values ($\sim$800 km) much differ from what was found in Figure 6a. We suspect a part of this discrepancy is explained by the regional variability of L_c (Rai et al., 2021), the other part is because of the way our co-spectrum is calculated: it makes use of a Hanning window that leads to under-estimate contributions of large time and spatial scales (see Appendix A). In terms of negative wind work, magnitude is -16 mW/m2. As a summary, considering positive and negative wind work in the Kuroshio-Extension region, the net wind-work is positive and equal to 36 mW/m2. Note that similar results have been found in other areas of the world ocean, such as the ACC, the Gulf Stream and tropical regions (see Figure 8)

The co-spectrum in the Kuroshio-Extension suggests that wind stresses with high-frequencies force internal gravity waves with the same frequencies through a resonance mechanism (Klein et al., 2004). As already discussed in the previous section, this resonant behavior has been further checked and revealed by offsetting the timing of wind stress from surface current by different time periods: 3, 6 and 12 hours. Not surprisingly, specific results in the Kuroshio (only shown for the 12 hour offset) indicate that the wind work in the region of near-inertial motions and internal gravity waves is strongly affected by this offset (see the comparison of Figures 7a and b): the wind work, instead of being positive, now displays alternately positive and negative values (Figure 7b) leading to a much smaller wind work for higher frequencies. The wind work that impacts low frequency motions is almost unchanged by the offset.

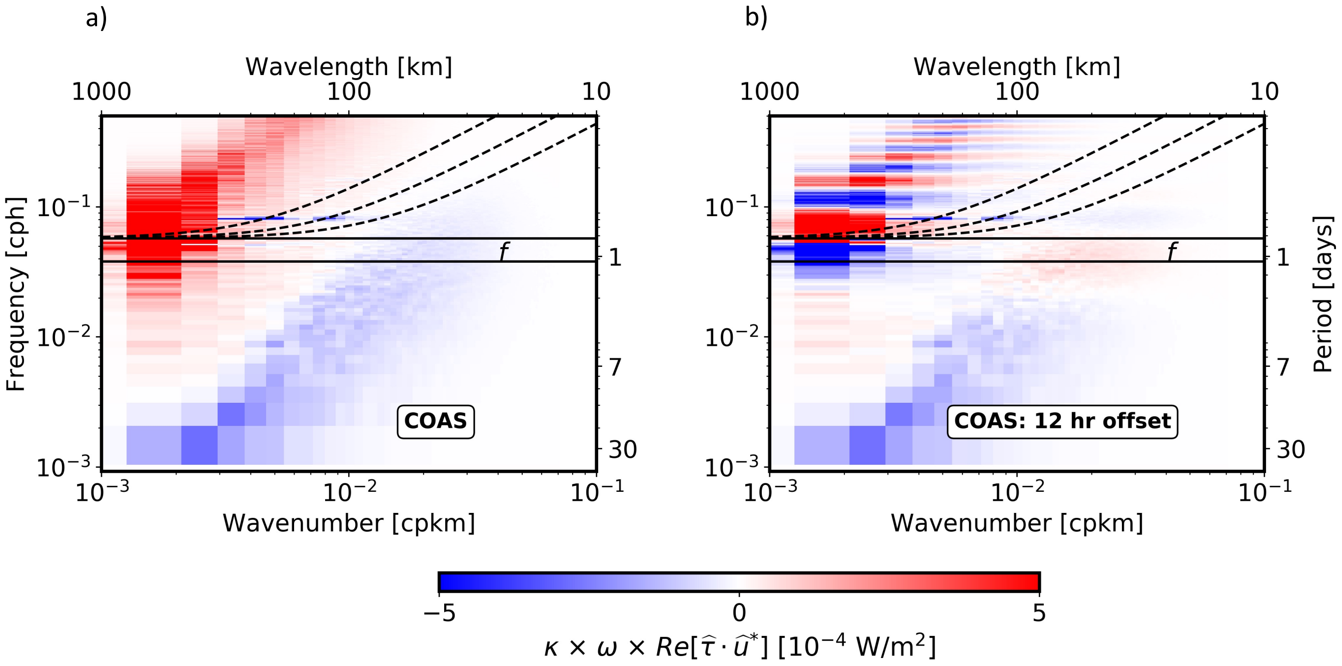

Figure 7. (a) co-spectrum of wind stresses and surface ocean currents in the Kuroshio Extension region from COAS simulation. (b) same as (a) except by offsetting wind stresses and surface currents by 12 hours. Using different offsettings (3 hours and 6 hours) produce the same results at 12 hours.

5 Discussion and Conclusion

The transfer of kinetic energy between the ocean and the atmosphere, the wind work, acts to force or damp ocean currents. Wind work diagnosis needs to consider wind stresses (and therefore winds) and surface ocean currents. These two variables occupy different regions in the spectral space. On the one hand, winds and wind stresses are usually energetic at high frequencies (<1-5 days) and large spatial scales (>500 km). On the other hand, except for a region within the near-inertial band that concerns large spatial scales, ocean currents are mostly energetic at lower frequencies with spatial scales smaller than 500 km, which corresponds to large and mesoscale eddies principally driven by the ocean interior dynamics. Since magnitude of ocean currents is at least one order of magnitude smaller than wind magnitudes, we expected and found large wind work magnitude in the near-inertial band and smaller wind work magnitude in the low frequency region. Wind work with specific time and spatial scales directly impacts ocean currents with the same scales. But it can indirectly impact ocean currents with different scales, through nonlinear advection terms, which emphasizes the need to consider wind work components, as defined in Eq. 4, altogether and not separately. The next paragraphs discuss our results.

First, we have estimated the impact of wind fluctuations with time scales smaller than 6 hours by comparing the wind work from our global coupled ocean-atmosphere model to the wind work from an ocean-only model forced by 6-hourly ECMWF

https://doi.org/10.5194/egusphere-2022-294
Preprint. Discussion started: 25 May 2022

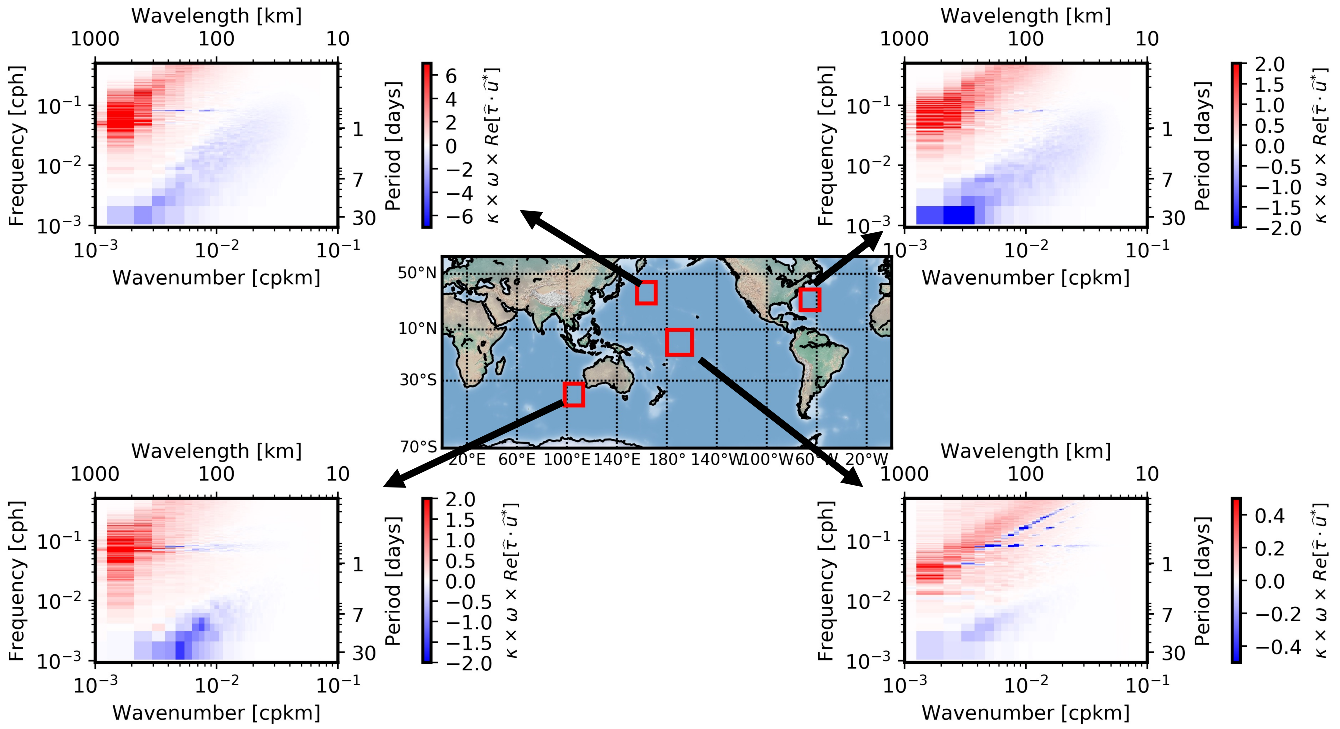

Figure 8. Co-spectrum of wind stresses and surface ocean currents in several regions from the COAS simulation (see square boxes in the middle panel). Note the color range is different in each panel.

winds. The global wind work in the coupled model is found to be larger than in the ocean-only model by a factor 1.6: reaching 5.21 TW instead of 2.98 TW. This increase is explained by the quadratic relationship between wind and wind stress as already pointed out by Zhai (2017). Second, as discussed below, an analysis, carried out by splitting the wind work into a time-mean component (43% of the total wind work) and a time-dependent component (57% of the total wind work) using a time period of 3.5 months, reveals that these components are strongly geographically dependent. We have analysed four wind work components, each one concerning a specific range of time and spatial scales (see Eq. 4).

The high-frequency component of the wind work dominates the time-dependent part of the wind work since its magnitude is larger than the low-frequency components by a factor ∼3. We found that this high-frequency component is mostly located at mid-latitudes in the region of atmospheric storm tracks. It directly forces internal gravity waves, and principally near-inertial waves with large spatial scales. Usually, the resulting near-inertial waves interact (through the nonlinear advection terms) with motions with lower frequencies and smaller spatial scales, such as mesoscale eddy motions, leading to internal waves with smaller spatial scales (Kunze, 1985; Young and Jelloul, 1997; Klein et al., 2019). The resulting waves are known to quickly propagate into the ocean interior, down to 2000-3000 m, where they contribute to ocean mixing (Komori et al., 2008; Danioux et al., 2011). Such propagation of near-inertial waves down into the ocean interior was not examined in our study. It was investigated in a coupled simulation with low spatial resolution by Komori et al. (2008) and needs to be revisited in a future study using our high-resolution coupled simulation. Compared with Komori et al. (2008), we expect an intensification of this mechanism due to the higher spatial resolution.

The two low-frequency components impact large eddies and mesoscale eddies, known to explain more than 80% of the total kinetic energy in the ocean (Ferrari and Wunsch, 2009) and to be mostly driven by the ocean interior dynamics and in particular by baroclinic instabilities (Tulloch et al., 2011; Klein et al., 2019). These eddies explain most of the upward vertical heat transport in the oceans and drive the meridional heat transport from the equator to the poles. The low-frequency components are dominant at mid-latitudes, where large and mesoscale eddies are the most energetic and, to a lesser extent, in the equatorial and tropical bands where low-frequency motions are mostly tropical waves. Wind work corresponding to scales smaller than 275 km is negative at mid-latitudes indicating it acts as an eddy damping for mesoscale eddies with these sizes. The eddy damping paradigm has been well discussed in the litterature (Eden and Dietze, 2009) and more recently by Renault et al. (2016) and Renault et al. (2018). This negative part of the low-frequency wind work has been found to be smaller, by a factor of 10 than the positive part explained by scales larger than 275 km, the latter acting as to force large eddies. However, we expect that, because of the nonlinear advection terms discussed through eqs. 5 and 6 in Section 3, instabilities of the resulting large eddies may energize smaller eddies and therefore counteract the eddy damping effect mentioned before. Reciprocally, smaller eddies can energize larger eddies through the inverse kinetic energy cascade which is also a consequence of the impact of nonlinear advection terms. This comment emphasizes that these two low-frequency components of the wind cannot be examined separately and their examination should include the impact of nonlinear advection terms. This point should be the focus of a future study.

The time-mean component was found to be significant only in the equatorial/tropical regions and also in the southern hemisphere. This component mostly forces equatorial and tropical zonal jets. It may also force tropical wave instabilities, through the nonlinear advection terms, but this has never been investigated to our knowledge. The large wind forcing in the southern hemisphere should affect stationary eddies. This is also something to further examine. A more precise interpretation of this time-mean component requires to analyse a longer coupled simulation. Indeed, the 3.5 month period is also the time scale of large eddies. Considering a longer time period, such as a year, will help to better discriminate between large eddies and mean currents like equatorial and tropical jets. Our simulation has been recently run on a longer period. So, we hope to address this issue in the next future.

Results of this study, in particular those in spectral space, emphasize the importance of taking into account high-resolution ocean currents and wind stresses (with time scales of one hour and spatial scales of 15 km) to estimate the wind work. Indeed, results indicate that high-resolution currents and wind stresses significantly impact the zonal jets in tropical and equatorial regions, mean currents and ocean eddies at mid-latitudes as well as near-inertial motions and internal gravity waves. The recent and next generations of atmosphere-ocean coupled models will help to estimate not only the wind work but also the nonlinear advection terms, i.e. the kinetic energy budget in the upper ocean.

Our results further emphasize the need to have satellite observations of wind stresses and currents with a resolution of at least 10 km and a temporal resolution less than 12 hours. The present ASCAT wind observations and ocean currents diagnosed from conventional altimeters do not meet these requirements. However, several future projects, such as the Wind and Current mission (WaCM) (Rodríguez et al., 2019) and the Ocean Surface Current Multiscale Observation Mission (OSCOM) (Du et al., 2021), intend to address the strong limitations of existing wind and current products. Thus, WaCM aims to measure directly wind stresses and ocean surface currents with sensors on-board on only one satellite, with a spatial and time resolution never attained so far ($\sim$ 10 km, twice a day). In addition to be collocated and contemporaneous, these global measurements of wind stress and ocean current will have wide-swaths as large as $\sim 1{,}800$ km, which represents a major breakthrough. Furthermore, observations from the upcoming Surface Water and Ocean Topography mission (SWOT) should give access to geostrophic currents with a resolution of $\sim$15 km over a wide-swath of 120 km. We envision that these future observations, exploited in combination with SST observations from Advanced Microwave Scanning Radiometer (AMSR-E) will permit to estimate not only the kinetic energy budget (including the wind work and the nonlinear advection of momentum), as suggested by the present study, but also the heat budget in the upper ocean (Klein et al., 2019). In anticipation, modelling studies like the present one should help to better assess the potential of these missions.

Appendix A: Frequency-wavenumber spectrum and co-spectrum

The ω-κ spectrum of a given variable $\phi(x,y,t)$ is computed in a domain 1000 km-size and over 90 days. We refer the reader to Torres et al. (2018) for the full methodology. Briefly, before computing the ω-k spectrum of a $\phi(x,y,t)$, its linear trend is removed and a 3-D Hanning window is subsequently applied to the de-trended $\phi(x,y,t)$ (Qiu et al., 2018). A discrete 3-D Fourier transform is then computed to retrieve $\hat{\phi}(k,l,\omega)$ the Fourier coefficients, where $\hat{.}$ is the Fourier transform, k the zonal wavenumber, l the meridional wavenumber, and ω the frequency. Finally, the 3-D Fourier transform is used to compute a 2-D spectral density, $|\hat{\phi}|^2(\kappa,\omega)$ where κ is the isotropic wavenumber defined as $\kappa = \sqrt{k^2+l^2}$. The transformation from an anisotropic spectrum to an isotropic spectrum is performed following the methodology described by Torres et al. (2018).

The co-spectrum of the wind work is computed similarly to the ω-κ spectrum, following the methodology described in Flexas et al. (2019). First, the Fourier transforms of the wind stress $\hat{\tau}(k,l,\omega)$ and ocean current $\widehat{\mathbf{u_o}}(k,l,\omega)$ are calculated. The co-spectrum of the wind work is then given by

$$\widehat{\boldsymbol{\tau}.\mathbf{u_o}}\,(k,l,\omega) = Re\left[\widehat{\boldsymbol{\tau}}.\widehat{\mathbf{u_o}}^*\,(k,l,\omega)+\widehat{\boldsymbol{\tau}}^*.\widehat{\mathbf{u_o}}\,(k,l,\omega)\right]$$

where Re is the real part of the complex quantity, and asterisk (*) the complex conjugate. The 2-D co-spectrum, $\widehat{\boldsymbol{\tau}.\mathbf{u_o}}(\kappa,\omega)$, is retrieved using the same methodology as before.

The ω-κ spectrum and co-spectrum are presented in a variance preserving form for easier comparison across the frequency-wavenumber domain.

Appendix B: Momentum budget in the upper oceanic layers

Let us assume a constant mixed-layer depth, H, for the sake of simplicity. Wind stress, $\boldsymbol{\tau}$, will force surface currents, $\mathbf{u_o}$, following

$$\frac{\partial \mathbf{u_o}}{\partial t} \sim \frac{\tau}{H} \tag{B1}$$

Using $\mathbf{u_o} = \overline{\mathbf{u_o}} + \mathbf{u}_{\mathbf{o}}^{'}$ and $\boldsymbol{\tau} = \overline{\boldsymbol{\tau}} + \tau^{'}$, with overline being a time-average operator over 3.5 months, leads to

$$\frac{\partial \overline{\mathbf{u_o}} + \mathbf{u}_{\mathbf{o}}^{'}}{\partial t} \sim \frac{\overline{\boldsymbol{\tau}} + \tau^{'}}{H}\,. \tag{B2}$$

Time-averaging Eq. B2 and multiplying the resulting equation by $\overline{\mathbf{u_o}}$ yields

$$\frac{\partial \overline{\mathbf{u_o}^{\mathbf{2}}}/2}{\partial t} \sim \frac{\overline{\tau}.\overline{\mathbf{u_o}}}{H}\,. \tag{B3}$$

After multiplying Eq. B2 by $\overline{\mathbf{u_o}} + \mathbf{u}_{\mathbf{o}}^{'}$ and taking the time average and using Eq. B3, we get

$$\frac{\partial \overline{\mathbf{u_o}'^{\mathbf{2}}}/2}{\partial t} \sim \frac{\overline{\boldsymbol{\tau}^{'}.\mathbf{u_o}'}}{H}\,. \tag{B4}$$

The same operation can now be done using $\mathbf{u_o}' = \mathbf{u_o}_{hf}^{'} + \mathbf{u_o}_{lf}^{'}$, which leads to

$$\frac{\partial \overline{\mathbf{u_o}_{hf}^{'2}}/2}{\partial t} \sim \frac{\overline{\boldsymbol{\tau}^{'}.\mathbf{u_o}_{hf}^{'}}}{H}\,, \tag{B5}$$

$$\frac{\partial \overline{\mathbf{u_o}_{lf}^{'2}}/2}{\partial t} \sim \frac{\overline{\boldsymbol{\tau}^{'}.\mathbf{u_o}_{lf}^{'}}}{H}\,. \tag{B6}$$

The same arguments, but now in spatial space, can be applied using $\mathbf{u_o}_{lf}^{'} = \mathbf{u_o}_{lf>}^{'} + \mathbf{u_o}_{lf>}^{'}$ leading to

$$\frac{\partial \overline{\mathbf{u_o}_{lf>}^{'2}}/2}{\partial t} \sim \frac{\overline{\boldsymbol{\tau}^{'}.\mathbf{u_o}_{lf>}^{'}}}{H}\,, \tag{B7}$$

$$\frac{\partial \overline{\mathbf{u_o}_{lf<}^{'2}}/2}{\partial t} \sim \frac{\overline{\boldsymbol{\tau}^{'}.\mathbf{u_o}_{lf<}^{'}}}{H}\,. \tag{B8}$$

Thus, from eqs. B3, B5, B6, B7, and B8, each term on the RHS of Eq. 4, related to a given fluctuation class, directly forces surface currents corresponding to the same class. Results above can also be understood if moving to the spectral space, since Eq. B1 becomes

$$\frac{\partial \widehat{\mathbf{u_o}}(\omega,k)}{\partial t} \sim \frac{\widehat{\tau}(\omega,k)}{H}\,. \tag{B9}$$

leading to

$$\frac{\partial|\widehat{\mathbf{u_o}}(\omega,k)|^2/2}{\partial t} \sim \frac{\Re[\widehat{\tau}(\omega,k).\widehat{\mathbf{u_o}}^*(\omega,k]}{H}\,. \tag{B10}$$

with $\widehat{.}$ the Fourier transform, * the conjugate, ω the frequency, k the wavenumber and $\mathcal{R}$ the real part. So, each frequency and each wavenumber of the wind stress forces surface currents with the same frequency and wavenumber.

However, the full momentum equations, including nonlinear advection terms, highlight that fluctuating wind stresses indirectly force mean surface currents and, similarly, mean wind stresses force fluctuating surface currents. These nonlinear effects are illustrated below.

Let us start with the full momentum equations

$$\frac{\partial \mathbf{u_o}}{\partial t} \sim -\mathbf{u_o}\cdot\nabla\mathbf{u_o} + \frac{\tau}{H}\,. \tag{B11}$$

Applying for example the decomposition $\mathbf{u_o} = \overline{\mathbf{u_o}} + \mathbf{u_o}'$ and $\boldsymbol{\tau} = \overline{\boldsymbol{\tau}} + \tau'$ to Eq. B11 leads, after some calculations, to

$$\frac{\partial\overline{\mathbf{u_o}}^2/2}{\partial t} \sim -\overline{\mathbf{u_o}}\cdot\overline{\mathbf{u_o}}\cdot\nabla\overline{\mathbf{u_o}} - \overline{\mathbf{u_o}}\cdot\overline{\mathbf{u_o}'\cdot\nabla\mathbf{u_o}'} + \frac{\overline{\tau}\cdot\overline{\mathbf{u_o}}}{H}\,, \tag{B12}$$

$$\frac{\partial\overline{\mathbf{u_o}'^{\,2}}/2}{\partial t} \sim -\overline{\mathbf{u_o}'\cdot\mathbf{u_o}'}\cdot\nabla\overline{\mathbf{u_o}} - \overline{\mathbf{u_o}'\cdot\mathbf{u_o}'\cdot\nabla\mathbf{u_o}'} - \overline{\mathbf{u_o}}\cdot\overline{\mathbf{u_o}'\cdot\nabla\mathbf{u_o}'} + \frac{\overline{\boldsymbol{\tau}'.\mathbf{u_o}'}}{H}\,. \tag{B13}$$

From eqs. B12 and B13, the time-mean and fluctuations surface currents, resulting directly from the wind work forcing, subsequently interact through the nonlinear advection terms in the momentum equations. For example, fluctuating surface currents forced by wind stress fluctuations (Eq. B13) impact mean current through the second RHS term in Eq. B12. Similarly, mean current forced by mean wind stress (Eq.B12) impact current fluctuations through the first RHS term in Eq. B13 since these mean currents can be unstable. This example emphasizes that mean wind stress can force indirectly fluctuating currents and fluctuating wind stress can force indirectly mean currents. It confirms that the different components of the wind work displayed in Eq. 4 need to be considered altogether and not separately. Nonlinear interactions are more complex than shown in eqs. B12 and B13. This can be understood when moving again to the spectral space. Indeed, the generalization of Eq. B10 leads to

$$\frac{\partial|\widehat{\mathbf{u_o}}(\omega,k)|^2/2}{\partial t} \sim -\Re[(\widehat{\mathbf{u_o}.\nabla\mathbf{u_o}})(\omega,k).\widehat{\mathbf{u_o}}^*(\omega,k)] + \frac{\Re[\widehat{\tau}(\omega,k).\widehat{\mathbf{u_o}}^*(\omega,k]}{H}\,. \tag{B14}$$

where $\mathbf{u_o}$ in the term $\widehat{\mathbf{u_o}.\nabla\mathbf{u_o}}(\omega,k)$ involve frequencies (ω_1 and ω_2) and wavenumbers (k_1 and k_2) such that $\omega_1+\omega_2=\omega$ and $k_1+k_2=k$.

Code availability. ©. All rights reserved

Data availability. The coupled ocean-atmosphere simulation has different channels of distribution: 1) Accessible from any NASA Ames Supercomputer at `~dmenemen/c1440_llc2160`, 2) accessible via NASA Ames data portal: https://data.nas.nasa.gov/ecco/data.php, 3) accessible via xmitgcm: https://xmitgcm.readthedocs.io, 4) DYAMOND period accessible at NCCS, on NCCS data portal, and at https://www.esiwace.eu/services/dyamond-initiative/services-dyamond-winter

Author contributions. HT and PK led the data analysis and data interpretation and drafted the manuscript. DM, CNH, AM, and ES helped develop and integrate the forced-ocean and coupled ocean-atmosphere simulations. All authors contributed to the scientific interpretation of the results and reviewed the manuscript.

Competing interests. The authors declare that they have no conflict of interest.

Acknowledgements. This work was performed at the Jet Propulsion Laboratory, California Institute of Technology under prime contract with NASA QuikSCAT project. Copyright 2021 California Institute of Technology. US government sponsorship acknowledged. HT, JW, AW, ER, DM, HZ, and DPM were supported by the NASA Physical Oceanography (PO) and Modeling, Analysis, and Prediction (MAP) programs. PK acknowledges support from the SWOT Science Team, the NASA S-Mode project and the QuikSCAT mission. AFT and MF were supported by the NASA S-MODE project and PDRDF funding from NASA's Jet Propulsion Laboratory BQ acknowledges support from NASA OSTST project. High-end computing was provided by the NASA Advanced Supercomputing (NAS) Division at the Ames Research Center.

References

Alford, M. H., MacKinnon, J. A., Simmons, H. L., and Nash, J. D.: Near-inertial internal gravity waves in the ocean, Annual review of marine science, 8, 95–123, 2016.

Aluie, H.: Convolutions on the sphere: commutation with differential operators, GEM - International Journal on Geomathematics, 10, 1–31, 2019.

Arbic, B. K., Alford, M. H., Ansong, J. K., Buijsman, M. C., Ciotti, R. B., Farrar, J. T., Hallberg, R. W., Henze, C. E., Hill, C. N., Luecke, C. A., Menemenlis, D., Metzger, E. J., Müeller, M., Nelson, A. D., Nelson, B. C., Ngodock, H. E., Ponte, R. M., Richman, J. G., Savage, A. C., Scott, R. B., Shriver, J. F., Simmons, H. L., Souopgui, I., Timko, P. G., Wallcraft, A. J., Zamudio, L., and Zhao, Z.: A Primer on Global Internal Tide and Internal Gravity Wave Continuum Modeling in HYCOM and MITgcm, in: New Frontiers in Operational Oceanography, edited by Chassignet, E. P., Pascual, A., Tintoré, J., and Verron, J., chap. 13, pp. 307–392, GODAE OceanView, https://doi.org/10.17125/gov2018.ch13, 2018.

Chelton, D. B., Schlax, M. G., and Samelson, R. M.: Global observations of nonlinear mesoscale eddies, Progress in Oceanography, 91, 167–216, 2011.

Chen, R., Flierl, G. R., and Wunsch, C.: A description of local and nonlocal eddy–mean flow interaction in a global eddy-permitting state estimate, Journal of Physical Oceanography, 44, 2336–2352, 2014.

Danioux, E., Klein, P., Hecht, M. W., Komori, N., Roullet, G., and Le Gentil, S.: Emergence of wind-driven near-inertial waves in the deep ocean triggered by small-scale eddy vorticity structures, Journal of physical oceanography, 41, 1297–1307, 2011.

Du, Y., Dong, X., Jiang, X., Zhang, Y., Zhu, D., Sun, Q., Wang, Z., Niu, X., Chen, W., Zhu, C., et al.: Ocean surface current multiscale observation mission (OSCOM): Simultaneous measurement of ocean surface current, vector wind, and temperature, Progress in Oceanography, 193, 102 531, 2021.

Eden, C. and Dietze, H.: Effects of mesoscale eddy/wind interactions on biological new production and eddy kinetic energy, Journal of Geophysical Research: Oceans, 114, 2009.

Ferrari, R. and Wunsch, C.: Ocean circulation kinetic energy: Reservoirs, sources, and sinks, Annual Review of Fluid Mechanics, 41, 2009.

Flexas, M. M., Thompson, A. F., Torres, H. S., Klein, P., Farrar, J. T., Zhang, H., and Menemenlis, D.: Global Estimates of the Energy Transfer From the Wind to the Ocean, With Emphasis on Near-Inertial Oscillations, Journal of Geophysical Research: Oceans, 124, 5723–5746, https://doi.org/10.1029/2018JC014453, 2019.

Garfinkel, C. I., Molod, A. M., Oman, L. D., and Song, I.-S.: Improvement of the GEOS-5 AGCM upon updating the air-sea roughness parameterization, Geophysical Research Letters, 38, n/a–n/a, https://doi.org/10.1029/2011GL048802, l18702, 2011.

Helfand, H. M. and Schubert, S. D.: Climatology of the Simulated Great Plains Low-Level Jet and Its Contribution to the Continental Moisture Budget of the United States, Journal of Climate, 8, 784–806, https://doi.org/10.1175/1520-0442(1995)008<0784:COTSGP>2.0.CO;2, 1995.

Klein, P., Lapeyre, G., and Large, W.: Wind ringing of the ocean in presence of mesoscale eddies, Geophysical research letters, 31, 2004.

Klein, P., Lapeyre, G., Siegelman, L., Qiu, B., Fu, L.-L., Torres, H., Su, Z., Menemenlis, D., and Le Gentil, S.: Ocean-Scale Interactions From Space, Earth and Space Science, 2019.

Komori, N., Ohfuchi, W., Taguchi, B., Sasaki, H., and Klein, P.: Deep ocean inertia-gravity waves simulated in a high-resolution global coupled atmosphere–ocean GCM, Geophysical research letters, 35, 2008.

Kunze, E.: Near-inertial wave propagation in geostrophic shear, Journal of Physical Oceanography, 15, 544–565, 1985.

https://doi.org/10.5194/egusphere-2022-294
Preprint. Discussion started: 25 May 2022

Large, W. G. and Yeager, S. G.: Diurnal to decadal global forcing for ocean and sea-ice models: The data sets and flux climatologies, NCAR Tech Note NCAR/TN-460+STR, Boulder, Colo. Natl. Cent. for Atmos. Res., 434, 2004.

Large, W. G., McWilliams, J. C., and Doney, S. C.: Oceanic vertical mixing: A review and a model with a nonlocal boundary layer parameterization, Reviews of Geophysics, 32, 363–403, 1994.

Laurindo, L. C., Mariano, A. J., and Lumpkin, R.: An improved near-surface velocity climatology for the global ocean from drifter observations, Deep Sea Research Part I: Oceanographic Research Papers, 124, 73–92, 2017.

Maximenko, N. A., Oleg V., M., Pearn P., N., and Hideharu, S.: Stationary mesoscale jet-like features in the ocean, Geophysical research letters, 35, 2008.

Menemenlis, D., Campin, J.-M., Heimbach, P., Hill, C., Lee, T., Nguyen, A., Schodlok, M., and Zhang, H.: ECCO2: High resolution global ocean and sea ice data synthesis, Mercator Ocean Quarterly Newsletter, 31, 13–21, 2008.

Molod, A., Suarez, M., and Partyka, G.: The impact of limiting ocean roughness on GEOS-5 AGCM tropical cyclone forecasts, Geophysical Research Letters, 40, 411–416, https://doi.org/10.1029/2012GL053979, 2013.

Molod, A., Takacs, L., Suarez, M., and Bacmeister, J.: Development of the GEOS-5 atmospheric general circulation model: evolution from MERRA to MERRA2, Geoscientific Model Development, 8, 1339–1356, https://doi.org/10.5194/gmd-8-1339-2015, 2015.

Nikurashin, M., Vallis, G. K., and Adcroft, A.: Routes to energy dissipation for geostrophic flows in the Southern Ocean, Nature Geoscience, 6, 48–51, 2013.

Polzin, K. L. and Lvov, Y. V.: Toward regional characterizations of the oceanic internal wavefield, Reviews of geophysics, 49, 2011.

Qiu, B., Chen, S., Klein, P., Wang, J., Torres, H., Fu, L.-L., and Menemenlis, D.: Seasonality in transition scale from balanced to unbalanced motions in the world ocean, Journal of Physical Oceanography, 48, 591–605, 2018.

Rai, S., Hecht, M., Maltrud, M., and Aluie, H.: Scale of oceanic eddy killing by wind from global satellite observations, Science Advances, 7, eabf4920, https://doi.org/10.1126/sciadv.abf4920, 2021.

Renault, L., Molemaker, M. J., McWilliams, J. C., Shchepetkin, A. F., Lemarié, F., Chelton, D., Illig, S., and Hall, A.: Modulation of wind work by oceanic current interaction with the atmosphere, Journal of Physical Oceanography, 46, 1685–1704, 2016.

Renault, L., McWilliams, J., and Gula, J.: Dampening of Submesoscale Currents by Air-Sea Stress Coupling in the Californian Upwelling System, Scientific Reports, 8, 13 388, 2018.

Rimac, A., von Storch, J.-S., Eden, C., and Haak, H.: The influence of high-resolution wind stress field on the power input to near-inertial motions in the ocean, Geophysical Research Letters, 40, 4882–4886, 2013.

Rocha, C. B., Chereskin, T. K., Gille, S. T., and Menemenlis, D.: Mesoscale to Submesoscale Wavenumber Spectra in Drake Passage, Journal of Physical Oceanography, 46, 601–620, https://doi.org/10.1175/JPO-D-15-0087.1, 2016.

Rodríguez, E., Bourassa, M., Chelton, D., Farrar, J. T., Long, D., Perkovic-Martin, D., and Samelson, R.: The winds and currents mission concept, Frontiers in Marine Science, 6, 438, 2019.

Strobach, E., Molod, A., Trayanov, A., Forget, G., Campin, J.-M., Hill, C., and Menemenlis, D.: Three-to-Six-Day Air–Sea Oscillation in Models and Observations, Geophysical Research Letters, 47, e2019GL085 837, https://doi.org/10.1029/2019GL085837, e2019GL085837 10.1029/2019GL085837, 2020.

Strobach, E., Klein, P., Molod, A., Fahad, A. A., Trayanov, A., Menemenlis, D., and Torres, H.: Local Air-Sea Interactions at Ocean Mesoscale and Submesoscale in a Western Boundary Current, Geophysical Research Letters, 49, 1–10, https://doi.org/10.1029/2021GL097003, 2022.

https://doi.org/10.5194/egusphere-2022-294
Preprint. Discussion started: 25 May 2022

Su, Z., Wang, J., Klein, P., Thompson, A. F., and Menemenlis, D.: Ocean submesoscales as a key component of the global heat budget, Nature communications, 9, 775, 2018.

Torres, H. S., Klein, P., Menemenlis, D., Qiu, B., Su, Z., Wang, J., Chen, S., and Fu, L.-L.: Partitioning ocean motions into balanced motions and internal gravity waves: A modeling study in anticipation of future space missions, Journal of Geophysical Research: Oceans, 123, 8084–8105, 2018.

Tulloch, R., Marshall, J., Hill, C., and Smith, K. S.: Scales, growth rates, and spectral fluxes of baroclinic instability in the ocean, Journal of Physical Oceanography, 41, 1057–1076, 2011.

Yang, H., Wu, L., Chang, P., Qiu, B., Jing, Z., Zhang, Q., and Chen, Z.: Mesoscale Energy Balance and Air–Sea Interaction in the Kuroshio Extension: Low-Frequency versus High-Frequency Variability, Journal of Physical Oceanography, 51, 895–910, 2021.

Young, W. and Jelloul, M. B.: Propagation of near-inertial oscillations through a geostrophic flow, Journal of marine research, 55, 735–766, 1997.

Zhai, X.: On the wind mechanical forcing of the ocean general circulation, Journal of Geophysical Research: Oceans, 118, 6561–6577, 2013.

Zhai, X.: Dependence of energy flux from the wind to surface inertial currents on the scale of atmospheric motions, Journal of Physical Oceanography, 47, 2711–2719, 2017.

Zhai, X., Johnson, H. L., Marshall, D. P., and Wunsch, C.: On the wind power input to the ocean general circulation, Journal of Physical Oceanography, 42, 1357–1365, 2012.